Author(s): Montes, Plaza Adrian; Pakarinen, Janne; Papadakis, Philippos; Herzberg, Rolf-Dietmar; Julin, Rauno; Rodríguez, R.; Briscoe, Andrew D.; Illana, Andrés; Ojala, Joonas; Ruotsalainen, Panu; Uusikylä, Eetu; Alayed, Betool; Alharbi, Ahmed; Alonso-Sañudo, Odette; Auranen, Kalle; Bogdanoff, Ville; Chadderton, Jamie; Esmaylzadeh, Arwin; Fransen, Christoph; Grahn, Tuomas; Greenlees, Paul T.;

Title: Direct measurement of three different deformations near the ground state in an atomic nucleus

Year: 2025

Version: Published version

Please cite the original version:

Montes, P. A., Pakarinen, J., Papadakis, P., Herzberg, R.-D., Julin, R., Rodríguez, R., Briscoe, A. D., Illana, A., Ojala, J., Ruotsalainen, P., Uusikylä, E., Alayed, B., Alharbi, A., Alonso-Sañudo, O., Auranen, K., Bogdanoff, V., Chadderton, J., Esmaylzadeh, A., Fransen, C., . . . Zimba, G. L. (2025). Direct measurement of three different deformations near the ground state in an atomic nucleus. Communications Physics, 8, Article 8. https://doi.org/10.1038/s42005-024-01928-8

communications physics

Article

https://doi.org/10.1038/s42005-024-01928-8

Direct measurement of three different deformations near the ground state in an atomic nucleus

Adrian Montes Plaza[1,2], Janne Pakarinen[2] ✉, Philippos Papadakis[3], Rolf-Dietmar Herzberg[1], Rauno Julin[2], Tomás R. Rodríguez[4], Andrew D. Briscoe[2,11], Andrés Illana[2,4], Joonas Ojala[2], Panu Ruotsalainen[2], Eetu Uusikylä[2], Betool Alayed[1,5], Ahmed Alharbi[1,5], Odette Alonso-Sañudo[4], Kalle Auranen[2], Ville Bogdanoff[2], Jamie Chadderton[1], Arwin Esmaylzadeh[6], Christoph Fransen[6], Tuomas Grahn[2], Paul T. Greenlees[2], Jan Jolie[6], Henna Joukainen[2], Henri Jutila[2], Casper-David Lakenbrink[6], Matti Leino[2], Jussi Louko[2], Minna Luoma[2,7], Adam McCarter[1], Bondili Sreenivasa Nara Singh[8], Panu Rahkila[2], Andrea Raggio[2], Jorge Romero[1,2], Jan Sarén[2], Maria-Magdalini Satrazani[1,12], Marek Stryjczyk[2], Conor M. Sullivan[1], Álvaro Tolosa-Delgado[2,13], Juha Uusitalo[2], Franziskus von Spee[6], Jessica Warbinek[9,10,13] & George L. Zimba[2,14]

Atomic nuclei serve as prime laboratories for investigations of complex quantum phenomena, where minor nucleon rearrangements cause significant structural changes. ^{190}Pb is the heaviest known neutron-deficient Pb isotope that can exhibit three distinct shapes: prolate, oblate, and spherical, with nearly degenerate excitation energies. Here we report on the combined results from three state-of-the-art measurements to directly observe these deformations in ^{190}Pb. Contrary to earlier interpretations, we associate the collective yrast band as predominantly oblate, while the non-yrast band with higher collectivity follows characteristics of more deformed, predominantly prolate bands. Direct measurement of the $E0(0_2^+ \rightarrow 0_1^+)$ transition and γ-e^- coincidence relations allowed us to locate and firmly assign the 0_2^+ state in the level scheme and to discover a spherical 2_3^+ state at 1281(1) keV with $B(E2; 2_3^+ \rightarrow 0_1^+) = 1.2(3)$ W.u. These assignments are based purely on observed transition probabilities and monopole strength values, and do not rely on model calculations for their interpretation.

Since Morinaga proposed more than six decades ago that the excited 0_2^+ state in the ^{16}O nucleus was deformed[1], a large body of experimental evidence has been collected to demonstrate that atomic nuclei can possess different shapes[2]. Apart from the lightest elements, shape coexistence has been suggested to be present in all nuclei[3] and the competition of different configurations can result in several different shapes within the same nucleus[4]. Nevertheless, coexistence of three or more total energy minima near the ground state have been predicted to occur in only few regions in the chart of nuclei[5], but direct experimental proof remained to be obtained. A notable example to date is the $^{186}Pb_{104}$ nucleus, where the three lowest-energy states are 0^+ states, each assigned with a different shape – namely spherical, prolate and oblate[6,7]. The ^{186}Pb nucleus lies at the heart of the neutron-deficient Pb region, which has been a subject for numerous theoretical and experimental investigations[3,8–11]. Within the mean-field picture, the total energy curve along the quadrupole deformation shows spherical, prolate and oblate minima close in energy. These minima are related to the

[1]Oliver Lodge Laboratory, University of Liverpool, Liverpool, UK. [2]Accelerator Laboratory, Department of Physics, University of Jyväskylä, Jyväskylä, Finland. [3]Nuclear Physics Group, STFC Daresbury Laboratory, Warrington, Cheshire, UK. [4]Grupo de Física Nuclear (GFN) and IPARCOS, Universidad Complutense de Madrid, CEI Moncloa, Madrid, Spain. [5]Department of Physics, College of Science, Qassim University, Buraydah, Saudi Arabia. [6]Universität zu Köln, Mathematisch-Naturwissenschaftliche Fakultät, Institut für Kernphysik, Köln, Germany. [7]Helsinki Institute of Physics, Helsinki, Finland. [8]School of Computing, Engineering and Physical Sciences, University of the West of Scotland, Paisley, UK. [9]GSI Helmholtzzentrum für Schwerionenforschung, Darmstadt, Germany. [10]Department Chemie - Standort TRIGA, Johannes Gutenberg - Universität, Mainz, Germany. [11]Present address: Oliver Lodge Laboratory, University of Liverpool, Liverpool, UK. [12]Present address: Instituut voor Kern- en Stralingsfysica, KU Leuven, Leuven, Belgium. [13]Present address: European Organisation for Nuclear Research (CERN), Geneva, Switzerland. [14]Present address: Facility for Rare Isotope Beams, Michigan State University, East Lansing, MI, USA. ✉e-mail: janne.pakarinen@jyu.fi

spherical $Z = 82$ shell gap, and prolate and oblate deformed gaps in the proton and neutron Nilsson orbitals, respectively. From a shell model perspective, the deformed minima (noted as $\pi(h^4_{9/2})$ for prolate and $\pi(h^2_{9/2})$ for oblate in the present work) are expected to have a complex spherical multiparticle-multihole configuration both for protons and neutrons[10–12]. Similar competition of different configurations is present in neighbouring isotopes around the $N = 104$ midshell[13]. In ^{188}Pb, in addition to low-lying deformed bands associated with predominantly prolate and oblate shapes[14–16], three isomeric states assigned with different shapes[17,18] have been proposed.

Intruding structures built on different configurations have also been observed in nuclei in the region around ^{186}Pb. In fact, the shape staggering of Hg isotopes observed in an isotopic shift experiment was a groundbreaking discovery in the 1970's[19] that triggered multiple investigations into shape coexistence. Laser spectroscopic measurements have examined the onset of ground-state deformation also in the even-mass Po and Pt isotopes[20,21]. Since the neutron-deficient Pb isotopes are spherical in their ground states[22–24], the onset of deformation in the Pb isotopes can be assessed by investigating the 2^+_1 states. It is proposed that the heaviest Pb nucleus exhibiting collectivity associated with deformation is ^{194}Pb[25], whereas in heavier Pb isotopes the underlying configurations of the lowest excited states arise from single-nucleon excitations in the seniority scheme leading to a spherical interpretation[26]. Despite the assignment of proposed oblate bands in Pb nuclei relying on comparisons with neighbouring nuclei and theoretical predictions, direct experimental evidence—such as measured quadrupole moments – has not yet been obtained. Similarly, the only direct experimental evidence for a prolate structure in Pb nuclei is the strongly-coupled band in ^{185}Pb[27].

The discovery of the ^{190}Pb nucleus was reported by Eskola[28] in 1967, but it took more than a decade until transitions between excited states were identified by Roulet et al.[29]. Inspired by a paper by May et al.[30], they discussed a transition from spherical to quadrupole deformed shape at low excitation energy, but without robust evidence, claims for axial deformation in this nucleus could not be made. The excited 0^+_2 state at 669(9) keV was observed in an α-decay fine structure measurement of ^{194}Po and assigned as an intruder proton-pair excitation across the $Z = 82$ closed shell and an oblate shape[31]. This finding paved the way for another ^{194}Po α-decay experiment, where a more precise value of 658(4) keV for the 0^+_2 level energy and a limit for its lifetime were determined through a direct measurement of conversion electrons in coincidence with α particles[32]. The latter allowed extracting a limit of $\rho^2 > 6 \times 10^{-3}$ for the monopole strength of the $E0(0^+_2 \rightarrow 0^+_1)$ transition, consequently assessing mixing between the deformed intruder 0^+_2 state and the spherical 0^+_1 ground state. A more complete level scheme was established in an in-beam spectroscopic study employing a germanium-detector array and a fusion-evaporation reaction by Dracoulis et al.[33]. In addition to three isomeric states, they found evidence for a prolate non-yrast band and a sequence of negative parity odd-spin states bypassing the isomeric states. A similar reaction was later used in a Gammasphere experiment by Wilson et al., who discovered a superdeformed band above the isomeric states[34].

In the present work, we combine results from three independent measurements on the ^{190}Pb nucleus employing two recoil separators in conjunction with state-of-the-art ancillary detector systems: 1) high-statistics recoil-gated prompt γ-γ and γ-electron coincidence spectroscopy; 2) recoil distance Doppler-shift lifetime measurements; and 3) delayed γ-ray spectroscopy following the de-excitation of isomeric states. These complementary experiments allowed us to extract many key transition properties and, consequently, to assign structures with specific shapes and the related configuration mixing with unprecedented precision. We report further proof for a predominantly prolate non-yrast band, reassign the yrast even-spin positive parity states to a predominantly oblate band and establish a candidate spherical 2^+_3 state. Our findings challenge the results of prevailing nuclear models and provide the first determination of monopole strengths of the inter-band transitions with non-zero angular momentum in neutron-deficient Pb nuclei.

Results

Experiments were performed in the Accelerator Laboratory of the University of Jyväskylä, Finland, employing the K130 cyclotron. Two different recoil separators were used to select fusion-evaporation residues (recoils in this work), whereas prompt and delayed spectrometers allowed for measuring transitions of interest at the target area and at the focal planes of the separators, respectively (see Methods for more details).

Prompt and delayed spectroscopy

Prompt recoil-gated γ-ray and electron energy spectra obtained in the present work contained ^{189,190}Pb and ^{189,190}Tl nuclei, as presented in Fig. 1a, b, respectively. Several new transitions were discovered, and their properties investigated through high-statistics γ-ray singles, electron singles, and γ-γ and γ-e^- coincidence analyses. A comprehensive understanding of the spectrometer properties[35,36] and measured γ-ray transitions allowed us to accurately predict the corresponding electron spectrum (see Fig. 1b). Confronting the expected with the measured electron spectra identified excess electron intensities which were assigned to $E0$ components in ^{189,190}Pb nuclei. Simultaneous observation of γ rays and electrons also allowed us to extract internal-conversion coefficients (ICC) for the most prominent transitions. Additionally, directional correlations from oriented states ratios (R_{DCO}) for several γ-ray transitions could be determined owing to the high granularity of the germanium-detector array. Transition properties obtained for ^{190}Pb are listed in Table S1. By means of coincidence relations, intensity balance arguments and extracted ICC and R_{DCO} values, the partial level scheme shown in Fig. 1c was constructed. The evidence for key discoveries and shape assignments are discussed below. Unless otherwise noted, all quoted uncertainties are 1σ.

Evidence for a new 1281 keV transition is present in Fig. 1a. Its placement in the level scheme is supported by Fig. 2a, which shows a recoil-gated γ-ray energy spectrum with a gate on 1281 keV γ rays. The presence of a few prominent peaks is apparent. The peak at 416 keV is identified as the $6^+_2 \rightarrow 4^+_2$ transition in ^{190}Pb. If the 1281 keV transition was above the 6^+_2 state, the most intense transitions below the 6^+_2 state should also appear in the spectrum. In contrast, other peaks are present, the most prominent one corresponding to a transition energy of 240(1) keV. Together with the 1281 keV transition, it forms a de-excitation path from the 1521 keV 4^+_2 state to the 0^+_1 ground state. In Fig. 2b, a recoil-gated γ-ray energy spectrum with a gate on the K-electrons of the 662 keV $0^+_2 \rightarrow 0^+_1$ transition shows a peak which we assign to the 619(2) keV transition originating from the new state at 1281(1) keV to the 0^+_2 state. To determine the spin of the 1281 keV state, we can rule out $J = 3$ as the measured lifetime would result in unrealistically fast $\Delta J = 3$ transitions to the 0^+ states. Similarly, a $J = 1$ assignment is excluded as the 240 keV transition from the 4^+_2 state would be weak and below the observational limit. Consequently, we report on the discovery of the new 2^+_3 state at 1281(1) keV, fed by the 240 keV $4^+_2 \rightarrow 2^+_3$ $E2$ transition and de-excited via the 1281 keV $2^+_3 \rightarrow 0^+_1$ and 619 keV $2^+_3 \rightarrow 0^+_2$ $E2$ transitions.

The measured R_{DCO} for the $2^+_2 \rightarrow 2^+_1$ and $4^+_2 \rightarrow 4^+_1$ inter-band transitions are not conclusive on either a pure $\Delta J = 1$ or $\Delta J = 2$ multipolarity (Table S1). However, the Clebsch-Gordan coefficient associated with a $M1$ component vanishes for such transitions between bands with $K = 0$ bandhead states[15]. The ICCs of $\Delta J = 0$ inter-band transitions from the 2^+_2 and 4^+_2 states were investigated using recoil-gated γ-ray and electron energy spectra with sum of gates on the γ rays from the $2^+_1 \rightarrow 0^+_1$ and $6^+_2 \rightarrow 4^+_2$ transitions, as shown in Fig. 3. The electron energy spectrum in panel **b** includes conversion electrons from the 455 keV $4^+_1 \rightarrow 2^+_1$ and 507 keV $6^+_1 \rightarrow 4^+_1$ yrast-band transitions. It also presents other peaks corresponding to the energies of the 389 keV $2^+_2 \rightarrow 2^+_1$ and 292 keV $4^+_2 \rightarrow 4^+_1$ inter-band transitions. The ICCs of these $\Delta J = 0$ inter-band transitions indicate the presence of strong $E0$ components.

Transitions below the isomeric 10^+_1 and 11^-_1 states with lifetimes of 216 ns and 11 μs[33], respectively, were studied at the MARA focal plane (recoil flight-time through MARA was ~1.35 μs). The results are included in Table S1, where intensities of transitions de-exciting the isomeric states have been normalised relative to the 338 keV $10^+_1 \rightarrow 8^+_2$ transition. Virtually

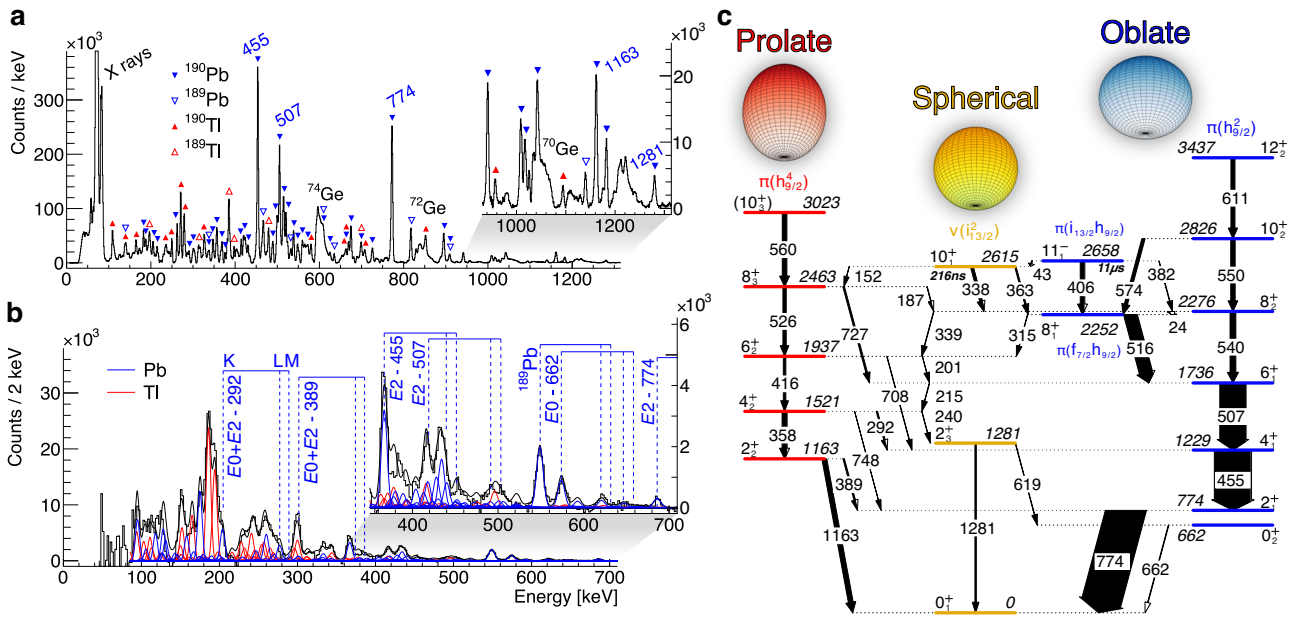

Fig. 1 | Recoil-gated background-subtracted prompt γ-ray and electron energy spectra obtained and partial level scheme of ^{190}Pb. a γ-ray energy spectrum in which the most prominent γ-ray peaks assigned with ^{190}Pb have been labelled with transition energies. Other peaks have been marked with different symbols and colours, according to the nucleus of origin. **b** electron energy spectrum. Calculated electron components are superimposed upon the measured spectrum. The black solid line presents the sum of all calculated electron components, whereas calculated components from different Pb and Tl nuclei are presented with blue and red colour, respectively. Positions of the K-, L- and M-conversion components of the most prominent $E2$ transitions in ^{190}Pb and the electron peaks corresponding to $E0$ transitions are marked. Close-ups of high-energy transitions are shown in the insets. **c** partial level scheme of ^{190}Pb. Levels assigned with predominantly spherical, oblate and prolate shape are coloured in yellow, blue and red, respectively, and are labelled with their predominant nucleon configuration. Vertical arrows represent transitions between states assigned with the same predominant intrinsic configuration, whereas diagonal arrows correspond to configuration-changing transitions. The widths of the arrows are proportional to the total transition intensities. Intensities of transitions from the 10^+_1 and 11^-_1 isomeric states have been balanced with intensities of de-exciting transitions from the states they feed.

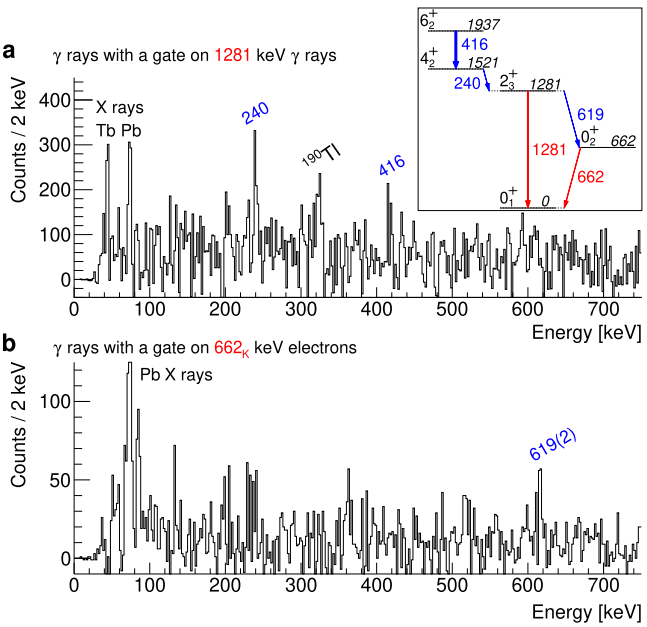

Fig. 2 | Recoil-gated background-subtracted prompt γ-ray energy spectra supporting the discovery of the third low-lying 2^+ state. a γ-ray energy spectrum gated on 1281 keV γ rays. The most prominent γ-ray peaks associated with ^{190}Pb have been labelled with transition energies. The partial level scheme is shown in the inset, with the gating transitions marked in red and the transitions in coincidence to those in blue. **b** γ-ray energy spectrum gated on K-conversion electrons from the $E0(0^+_2 \rightarrow 0^+_1)$ transition. New γ-ray peak is labelled with transition energy.

background-free γ-γ conditions, as demonstrated in the γ-ray energy spectrum in coincidence with the 1163 keV $2^+_2 \rightarrow 0^+_1$ γ rays in Fig. 4, lead to the discovery of new inter-band transitions. To allow for direct comparison in the level scheme (see Fig. 1c), intensities of transitions present in both prompt and delayed spectroscopy were normalised to prompt intensities using branching ratios. It is noteworthy, that transitions with intensities lower than a 5 per mille of the γ-ray intensity of the $2^+_1 \rightarrow 0^+_1$ transition could be observed.

Lifetime measurements

The lifetimes for ten excited states (see Table 1) were determined using the Bateman solutions of the radioactive decay equations[37] and the differential decay curve method (DDCM)[38]. The time evolution of γ-ray peaks was established by examining the intensity splitting at up to 12 plunger distances. This analysis accounts for emission of γ rays both before (I_{bd}) and after the degrader (I_{ad}). The decay curves were normalised with respect to the total γ-ray intensity using the quantity $R = I_{ad}/I_{tot} = I_{ad}/(I_{bd} + I_{ad})$.

The DDCM analysis with γ-γ coincidences was performed for the three lowest-lying yrast-band transitions. In the analysis, γ-γ matrices comparing the whole array versus each ring were constructed. The values reported for each ring are the average of the ones obtained using different gates. Thanks to the precise prompt and delay spectroscopy measurements we performed, the effect of unobserved feeding in the case of γ-ray singles measurement could be minimised in the DDCM analysis. While various hypotheses have been explored to account for unobserved feeding, the prevailing consensus is to assume the same average observed feeding time[38–40]. Due to insufficient statistics for feeding-transitions, the DDCM analysis could not be performed for the $8^+_1 \rightarrow 6^+_1$, $8^+_2 \rightarrow 6^+_1$, $10^+_2 \rightarrow 8^+_2$ and $6^+_2 \rightarrow 4^+_2$ transitions. Thus, corresponding decay curves were fitted using the Bateman equations. The adopted values represent the weighted averages based on the results obtained for each ring.

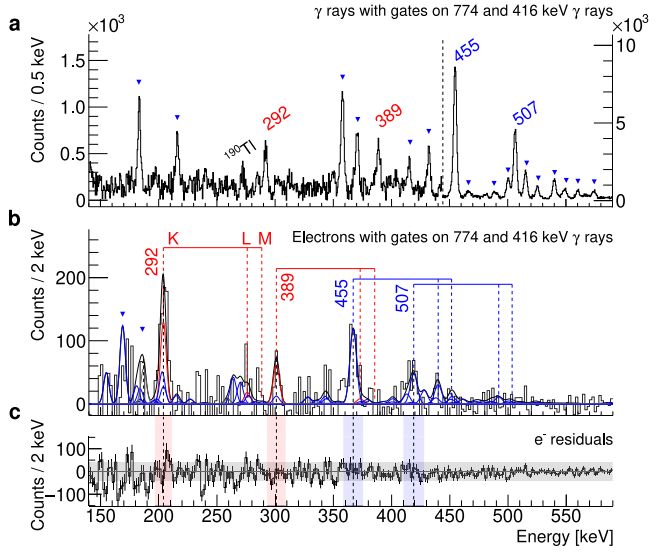

Fig. 3 | Recoil-gated background-subtracted prompt γ-ray and electron energy spectra with sum of gates on the 774 keV $2_1^+ \rightarrow 0_1^+$ and 416 keV $6_2^+ \rightarrow 4_2^+$ γ rays. The most prominent transitions have been marked with transition energy and the inter-band transitions are highlighted in red. Other transitions associated with ^{190}Pb are coloured in blue and marked with triangles. **a** γ-ray energy spectrum. **b** electron energy spectrum. Positions of the K-, L- and M-conversion components are marked. Calculated electron components are superimposed upon the measured spectrum in black. The red curves represent an excess of electrons and are identified as *E*0 components. **c** electron residuals spectrum showing the difference between the measured and calculated electron energy spectrum. The 3σ uncertainty of the residuals is shown as a gray band.

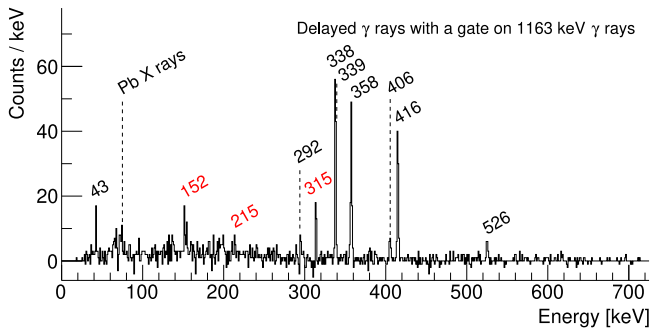

Fig. 4 | Recoil-gated background-subtracted delayed γ-ray energy spectrum measured at the MARA focal-plane. A gate on the 1163 keV $2_2^+ \rightarrow 0_1^+$ γ rays has been applied. The peaks are labelled according to transition energies (new transitions in red).

In the case of the 455 keV $4_1^+ \rightarrow 2_1^+$ transition, discrepancies were identified in the DDCM γ-γ analysis because of the contaminant transitions in the gates, whereas the DDCM analysis obtained with γ-ray singles data was also challenging due to multiple feeding transitions. Consequently, the adopted lifetime considers the spread of the results with both methods. It is noteworthy that the result obtained is consistent with a lifetime value of 8(3) ps obtained using the "gating from below" technique[41]. Examples of the lineshape and DDCM analysis performed for the three $2_i^+ \rightarrow 0_1^+$ transitions feeding the ground state are presented in Fig. 5. The case of the 774 keV $2_1^+ \rightarrow 0_1^+$ transition is shown for γ-γ analysis (ring 2) and in singles for the 1163 keV $2_2^+ \rightarrow 0_1^+$ and 1281 keV $2_3^+ \rightarrow 0_1^+$ transitions (ring 1).

Discussion

The transition properties extracted in the present work allowed for the firm assignment of transition multipolarities and fixed spins and parities for the states of interest. Together with measured lifetimes, reduced transition probabilities (referred to as *B*(*E*2) values from now on) were determined. In Table 2, these values are presented and grouped according to the predominant intrinsic configuration of the initial states. The *B*(*E*2) values played a crucial role in assigning states with specific configurations and deformations, as well as assessing configuration mixing. They have furthermore been compared to available theoretical calculations obtained within the interacting boson model (IBM) with configuration mixing[42], beyond-mean-field models using a Skyrme interaction[43] and a Gogny interaction performed in the present work, see Supplementary Note 1 and Figs. S1 and S2 for more details.

Table 1 | Mean lifetimes extracted for excited states in ^{190}Pb

J_i^π	E_i [keV]	τ [ps] Ring 1	τ [ps] Ring 2	$\tau_{adopted}$ [ps]
Spherical states				
2_3^+	1281	3.8(11)[a]	2.2(7)[a]	2.7(6)
Oblate states				
2_1^+	774	5.9(4)[b]	5.8(4)[b]	5.9(3)
4_1^+	1229	6.2(4)[a], 9.5(6)[b]	6.5(4)[a], 10.9(10)[b]	8.3(20)[c]
6_1^+	1736	3.9(6)[b]	2.1(4)[b]	3.0(9)[c]
8_1^+	2252	4.0(12)[d]	4.3(3)[d]	4.3(3)
8_2^+	2276	2.4(3)[d]	2.31(20)[d]	2.3(3)
10_2^+	2826	2.0(7)[d]	2.2(6)[d]	2.1(5)
Prolate states				
2_2^+	1163	6.9(5)[a]	7.1(4)[a]	7.0(3)
4_2^+	1521	10.1(5)[a]	10.5(5)[a]	10.3(4)
6_2^+	1937	4.2(7)[d]	3.1(4)[d]	3.4(3)

Spin, parity and energy of initial state and measured lifetimes are listed.
[a]Obtained from γ-ray singles data using DDCM.
[b]Obtained from γ-γ coincidence data using DDCM.
[c]The adopted value considers the spread between the rings.
[d]Obtained from γ-ray singles data using the Bateman analysis.

The *B*(*E*2) values obtained for the yrast and non-yrast band transitions suggest they are both collective, rotational bands (i.e. deformed). In the present work, the following equation has been employed to relate transition quadrupole moments $|Q_t|$ and quadrupole deformation parameters $|\beta_2|$:

$$|Q_t| = \frac{3}{\sqrt{5\pi}} Ze\left(1.2A^{1/3}\right)^2 |\beta_2| \,. \quad (1)$$

By using the determined *B*(*E*2) values, an average transition quadrupole moment $|Q_t|$ of 4.3(3) eb has been obtained for the intra-band transitions with $J_i^\pi > 2^+$ built on the lower-lying yrast states (see Fig. 6). This corresponds to a $|\beta_2|$ deformation of 0.147(10) and aligns with values determined for oblate bands in neighbouring nuclei[39]. From the intensity balances and lifetimes obtained for the 2_2^+ and 2_1^+ states, limits for the *B*(*E*2) values for unobserved transitions from the deformed 2^+ states to the 0_2^+ state could be determined. The $B(E2; 2_1^+ \rightarrow 0_2^+)$<290 W.u. value allows for a collective intra-band transition, whereas $B(E2; 2_2^+ \rightarrow 0_2^+)$<1 W.u. suggests the transition from the non-yrast band is hindered and not intra-band. Thus, the excited 0_2^+ state is assigned as the head of the predominantly oblate $\pi(h_{9/2}^2)$ band, fitting perfectly to the parabolic behaviour of oblate 0^+ level energy systematics[7]. This reassignment contrasts with the interpretation proposed by Dracoulis et al, who tentatively assigned the yrast even-spin states with a spherical shape[33], but finds support from many theoretical models[11,30,42–48].

The cascade of *E*2 transitions on top of the 1163 keV 2_2^+ state was discovered by Dracoulis et al.[33], who suggested an association with a prolate shape. Indeed, several theoretical calculations predict the existence of a prolate minimum in ^{190}Pb[11,30,42–49]. In the present study, average $|Q_t| = 6.35(22)$ eb and $|\beta_2| = 0.215(7)$ values were extracted for the two

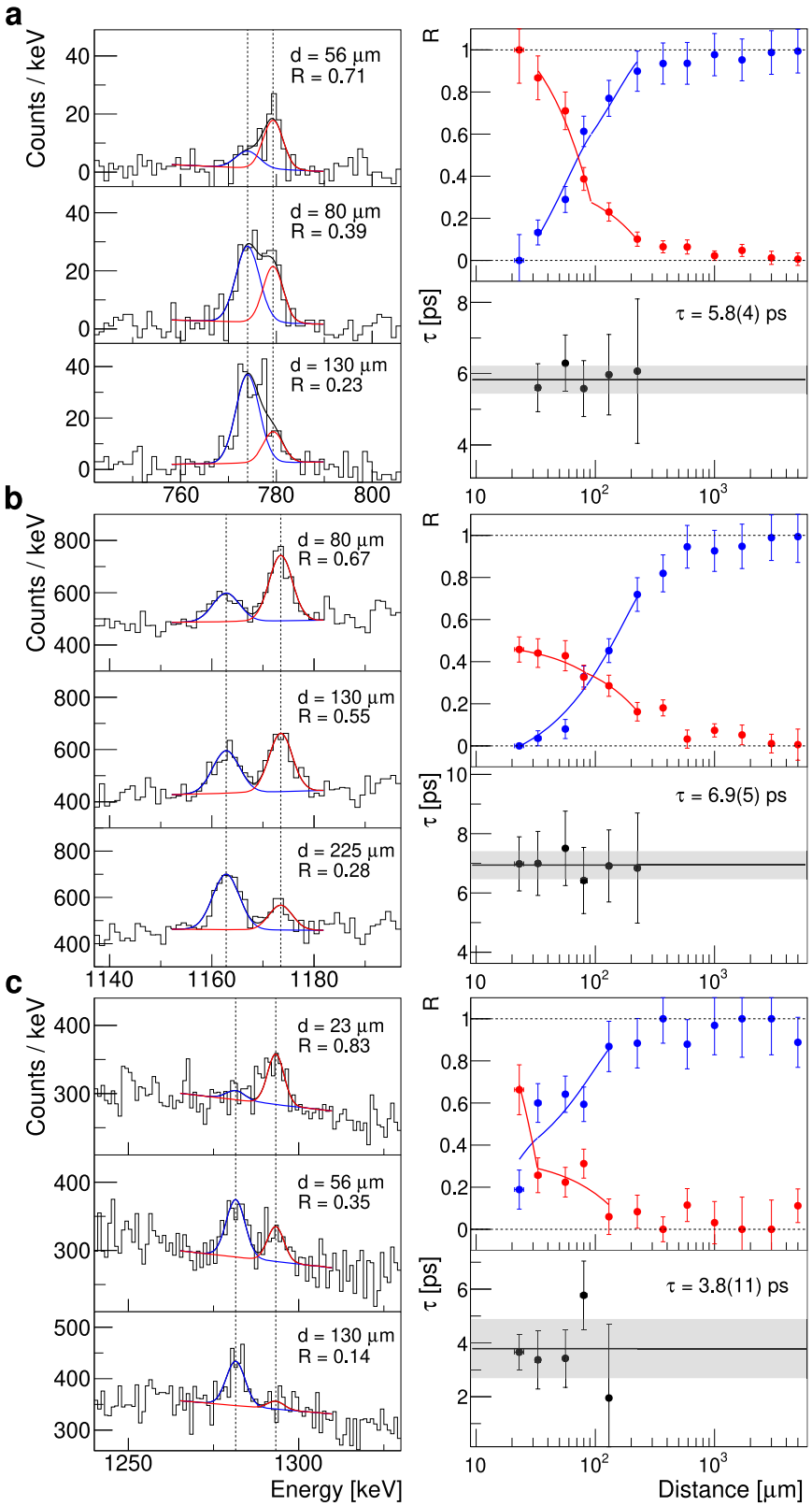

Fig. 5 | Sample plots illustrating the determination of lifetimes for the three 2^+ states using the differential decay curve method. For each transition, Doppler-corrected γ-ray energy spectra obtained for three different target-to-degrader distances are shown on the left, whereas the corresponding derivative and decay curve fits[38] are presented on the right. Data points shown in the right-hand panels are obtained from the measured components before and after the degrader, and are plotted in the same colour as displayed in the left panels. The error bars are dominated by statistical uncertainties. **a** results for the 774 keV $2_1^+ \rightarrow 0_1^+$ transition obtained from γ-γ coincidence data for ring 2. **b** results for the 1163 keV $2_2^+ \rightarrow 0_1^+$ transition obtained from γ-ray singles data for ring 1. **c** results for the 1281 keV $2_3^+ \rightarrow 0_1^+$ transition obtained from γ-ray singles data for ring 1. Target-to-degrader distances (d), intensity ratios (R) and average lifetimes (τ) obtained for each case are given.

non-yrast intra-band transitions with $J_i^\pi > 2^+$. The results indicate that the non-yrast band exhibits greater collectivity and deformation compared to the yrast band, offering additional evidence in support of the prolate assignment. It is noteworthy that the level energy spacing between prolate states in the Pb isotopes increases when moving towards heavier isotopes from the $N = 104$ midshell, (see e.g., Fig. 6 in Julin et al.[8]). This is a sign of reduced collectivity and is also reflected in smaller deformation, explaining slightly smaller $|Q_t|$ and $|\beta_2|$ values in ^{190}Pb nucleus than those obtained for prolate bands in ^{186,188}Pb nuclei. Increased deformation observed at the $N = 104$ midshell can be attributed to the multishell concept[4], which, when adjusted for the proton number Z, also explains the greater prolate deformation in ^{186}Pb compared to its lighter $N = 104$ isotones[8]. Based on the higher spin members of the prolate band, the level energy of the band-head 0_3^+ state is expected at around 1 MeV.

Table 2 | Comparison of the experimental *B*(*E*2) values to theoretical predictions in Weisskopf units

		E_γ	*B*(*E*2) values [W.u.]			
J_i^π	J_f^π	[keV]	This work	IBM	BMF_{Skyrme}	BMF_{Gogny}
Spherical $\nu(i^2_{13/2})$ initial state						
2_3^+	0_2^+	619	3.9(16)	–	6	4
	0_1^+	*1281*	*1.2(3)*	*16*	*5*	*23*
Oblate $\pi(h^2_{9/2})$ initial state						
10_2^+	8_2^+	*550*	*68(17)*	215	–	–
	8_1^+	574	39(10)	–	–	–
8_2^+	6_2^+	339	90(40)	–	–	<0.1
	6_1^+	*540*	*107(15)*	*211*	*191*	*193*
6_1^+	4_2^+	215	50(30)	–	<0.1	<0.1
	4_1^+	*507*	*120(40)*	*176*	*187*	*174*
4_1^+	2_1^+	*455*	*75(18)*	*76*	*149*	*150*
2_1^+	0_2^+	*112*	*<290*	*51*	*52*	*100*
	0_1^+	774	7.5(4)	3	10	3
Prolate $\pi(h^4_{9/2})$ initial state						
6_2^+	6_1^+	201	370(190)	107	5	<0.1
	4_2^+	*416*	*230(30)*	*223*	*393*	*408*
	4_1^+	708	2.7(9)	<1	0.5	< 0.1
4_2^+	4_1^+	292	68(8)	99	0.9	<0.1
	2_3^+	240	60(30)	73	20	5
	2_2^+	*358*	*142(9)*	*152*	*273*	*355*
	2_1^+	748	0.12(9)	39	0.2	<0.1
2_2^+	2_1^+	389	36(4)	85	5	<0.1
	0_2^+	501	<1	<1	1.3	0.1
	0_1^+	1163	0.65(4)	<1	1.3	0.1
Oblate $\pi(f_{7/2}h_{9/2})$ initial state						
8_1^+	6_2^+	315	25(8)	–	7	<0.1
	6_1^+	516	76(5)	–	–	<0.1

Interacting boson model (IBM)[42] and beyond-mean-field calculations (BMF) using a Skyrme interaction[43] are from literature, while beyond-mean-field calculations using a Gogny interaction were performed for the present work. Transitions have been organised in four groups that share the same predominant configurations in their initial states. Intra-band transitions are shown in italics.

The similarity of wavefunctions for states within a rotational band can be assessed by comparing the $|Q_t|^2$ values of the sequential intra-band transitions. The $|Q_t|$ value for both bands in ^{190}Pb increases when going from the 4^+ to 6^+ state (Fig. 6). Consequently, it is found that the predominantly prolate 2_2^+ state is 68(10)% composed of the configuration of the 4_2^+ state. Accordingly, the predominantly oblate 2_1^+ state has a 70(30)% component of the 4_1^+ state. Above the 6^+ state, the $|Q_t|$ values for the oblate band decrease. This is a sign of increased admixture of different configurations, which is also reflected in relatively high $B(E2)$ values for the inter-band transitions. In contrast to lighter Pb isotopes, transitions from the yrast to non-yrast band have also been observed. This demonstrates that the mixing of the two deformed bands extends at least up to $J^\pi = 8^+$.

The relatively strong feeding from the oblate 10_2^+ state to the 8_1^+ state suggests an overlap of initial and final state wavefunctions. This scenario was discussed by Dracoulis et al. who measured the *E*3 transition probabilities from the isomeric 11_1^- state, assigned with a $\pi(i_{13/2}h_{9/2})$ configuration and oblate shape, to different 8^+ states[50]. They concluded that the intrinsic configuration of the 8_1^+ state is a mixture of the $7/2^-[503]$ orbital originating from the $f_{7/2}$ configuration and the $7/2^-[514]$ deformation driving orbital from the $h_{9/2}$ configuration. The $B(E2; 8_1^+ \rightarrow 6_1^+) = 76(5)$ W.u. and $B(E2; 8_1^+ \rightarrow 6_2^+) = 25(8)$ W.u. values extracted in the present work support this interpretation.

The discovery of the 2_3^+ state at 1281 keV marks the first observation of the third excited 2^+ state in a Pb nucleus near the $N = 104$ midshell. The obtained $B(E2; 2_3^+ \rightarrow 0_1^+)$ value of 1.2(3) W.u. is close to the single-particle estimate, supporting the assignment with near-spherical shape. Calculations conducted using the quasiparticle random-phase approximation by Carlsson et al. predict the dominant neutron orbital component being $\nu(i^2_{13/2})$[51]. While the $B(E2; 2_3^+ \rightarrow 0_2^+) = 3.9(16)$ W.u. value indicates little mixing with the oblate $\pi(h^2_{9/2})$ configuration, the $B(E2; 4_2^+ \rightarrow 2_3^+) = 60(30)$ W.u. value suggests the 2_3^+ state has some prolate $\pi(h^4_{9/2})$ admixture.

Results from theoretical models presented in Table 2 and Fig. 6 are further considered in Fig. S2. They all predict three distinct total energy minima associated with (predominantly) spherical, oblate, and prolate shapes, in the same energy order. They also reproduce the increasing trend of $B(E2)$ and $|Q_t|$ values along the deformed bands up to $J^\pi = 6^+$. The IBM calculations, which had their mixing parameters refined to describe the measured $B(E2)$ values in ^{186}Pb and ^{188}Pb nuclei, exhibit the closest agreement with the experimental data regarding $B(E2)$ values and energy levels, albeit they overestimate the $B(E2)$ and $|Q_t|$ values for the oblate states above the 4_1^+ state. However, while the beyond-mean-field calculations predict too high level energies, particularly for spherical and prolate configurations, the $B(E2)$ and $|Q_t|$ values suggest they underestimate the amount of configuration mixing.

For the first time, the monopole strength (ρ^2) for transitions from states with non-zero angular momentum in the Pb isotopes were extracted in the present work. Consequently, very limited data exist for comparison. Monopole transition strengths have been determined via the relation: $\rho^2 = b_{E0}/(\tau\,\Omega_{E0})$, where b_{E0} is the ratio between the *E*0 intensity and the total intensity de-exciting the state, τ is the lifetime of the state and Ω_{E0} is the electronic factor for the *E*0 transition[52]. The $\rho^2(2_2^+ \rightarrow 2_1^+) = 17(7) \times 10^{-3}$ is close to those obtained within beyond-mean-field models using a Skyrme (42×10^{-3}) and a Gogny (24×10^{-3}) interaction. Regarding the measured $\rho^2(4_2^+ \rightarrow 4_1^+) = 19(6) \times 10^{-3}$, similar to the measured $\rho^2(2_2^+ \rightarrow 2_1^+)$ value, it is not reproduced by the beyond-mean-field models for which both provide much smaller values (Skyrme 1×10^{-3}, Gogny $\ll 1 \times 10^{-3}$). It is interesting to note that while the two-state mixing model[52,53] may be over-simplified for the current case, it provides a very similar estimate for mixing as inferred from the $B(E2)$ values. Taking the given $|\beta_2|$ deformations determined for oblate and prolate bands, the model predicts ~10% mixing between the oblate and prolate 2^+ and 4^+ states.

Conclusions

We have conducted direct measurements of three different deformations near the ground state in an atomic nucleus. These experiments took place at the Accelerator Laboratory of the University of Jyväskylä, Finland, during two separate beamtimes. The first experiment utilised the SAGE spectrometer[54] at the MARA vacuum-mode separator[55,56], while the second experiment used the JUROGAM 3 germanium-detector array[57] and a plunger device in conjunction with the RITU gas-filled separator[58,59]. Complementary delayed spectroscopy was performed during the first experiment. This approach serves as a textbook example of how a combination of different experimental techniques can give far-reaching insight into an exotic nucleus, such as ^{190}Pb. Drawing furthermore on the full body of experimental and theoretical data collected in this region, the different deformations can be associated with spherical, oblate, and prolate shapes. Confirmation of these shapes calls for a Coulomb excitation experiment employing radioactive ion beams that is sensitive to probe the signs of the quadrupole moments. Additionally, the 0^+ band-head state of the predominantly prolate band awaits discovery. To explore the intrinsic configurations of excited states using transfer reactions, advances in radioactive beam experiments are required. Finally, a comparison of results to theoretical models shows that while some measured features can be qualitatively

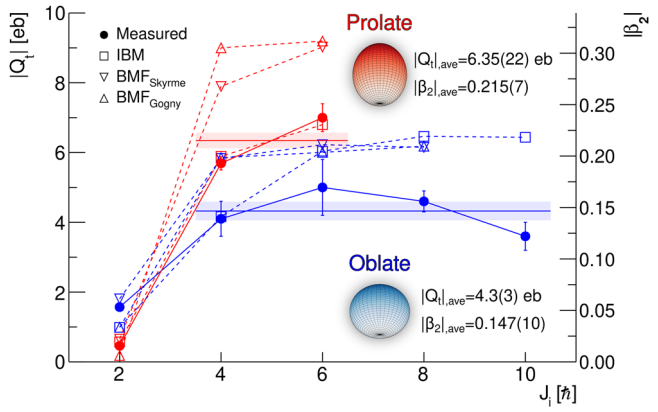

Fig. 6 | Transition quadrupole moments and deformation parameters as a function of angular momentum for the deformed bands in ^{190}Pb. The average transition quadrupole moment and deformation parameter calculated for each band with $J_i^\pi > 2_i^+$ are shown and represented as a line along with a shaded area corresponding to 1 σ uncertainty. The red and blue symbols correspond to values associated with the prolate and oblate bands, respectively. The error bars are dominated by the lifetime uncertainties. Interacting boson model (IBM) and beyond-mean-field (BMF) theoretical predictions using a Skyrme and a Gogny interaction are plotted for comparison.

Table 3 | Details of the performed experiments

	S24	JR161
Separator	MARA	RITU
Reaction	^{159}Tb (^{35}Cl, 4n)	^{108}Pd (^{86}Kr, 4n)
Beam energy	164 MeV	378 MeV
Average beam current	10 pnA	2 pnA
Beam charge-state	8^+	16^+
Irradiation time	320 h	250 h
Target thickness	0.35 mg cm^{-2}	~1 mg cm^{-2}
Degrader thickness	–	^{nat}Mg ~ 1 mg cm^{-2}
Prompt trigger width	2.5 μs	1.5 μs
Delayed trigger width	10 μs	8.5 μs

predicted, improved nuclear models are needed to quantitatively reproduce the observed data.

Methods

Data were obtained in two separate experiments, summarised in Table 3.

The simultaneous in-beam γ-ray and electron spectroscopy experiment (S24[60]) was part of the first campaign in which the silicon and germanium (SAGE) spectrometer[54] was used at the mass analysing recoil apparatus (MARA) vacuum-mode recoil separator[55,56]. The MARA separator allowed to discern recoils with different mass-over-charge ratios. The mass resolving power of MARA was sufficient to select fusion-evaporation products with $A = 189$ and 190 from other nuclei produced in the experiment. The MARA electric voltage and dipole magnetic field were optimised for transmission of ions in the 17^+ charge state.

The SAGE spectrometer is composed of the JUROGAM 3 spectrometer[57] for the measurement of γ rays around the production target and a 90-pixel silicon detector to measure conversion electrons. JUROGAM 3 comprises of 24 EUROGAM Clover and 10 EUROGAM Phase 1-type or GASP-type germanium detectors and their corresponding Compton-suppression shields. Prompt electrons were transported 955 mm's upstream from the target for detection, exploiting a magnetic field generated by solenoid coils operated with 850 A current. The δ-electron flux arising from the interaction of beam and target particles was suppressed by an electrostatic barrier applied to -32 kV potential.

The JR161[61] lifetime-measurement experiment was conducted employing the advanced plunger-particle detector array (APPA) in conjunction with 15 EUROGAM Phase-1 type germanium detectors (ten at $\theta = 133.6°$ and five at $\theta = 157.6°$ with respect to the beam axis) and the recoil ion transport unit (RITU) separator[58,59]. Twelve absolute target-to-degrader distances were selected in order to scan the lifetimes of interest appropriately, from 23(2) to 5000(10) μm, corresponding approximately to 2 and 400 ps recoils' time-of-flight.

The focal plane detector set-up was similar in both experiments. It consisted of a multiwire proportional counter (MWPC), a double-sided silicon strip detector (DSSD) of 192 vertical and 72 horizontal strips and 300 μm thickness, where recoils were implanted, and two so-called punch-through silicon detectors of 1 mm thickness to detect particles not depositing their full energy in the DSSD. Three broad energy germanium detectors (BEGe) were arranged around the DSSD for the collection of delayed γ rays. An additional Clover detector was used at the RITU focal plane in the JR161 experiment.

The total data readout data acquisition system[62] was used for data collection. Detector signals were timestamped with a global 100 MHz clock. The data were sorted using the MWPC energy signals as a trigger for in-beam and the DSSD energy signals for decay studies. The trigger window was comprised of a prompt and a delayed width in order to correlate in-beam and focal-plane signals, respectively, into the same event window. These widths were optimised for each experiment with the aim of maximising the delayed γ rays associated with a given recoil, while minimising the possibility of a subsequent recoil arriving during the previous trigger window. The time correlation of events was performed using the Grain[63] software package, whereas the ROOT framework[64] was employed for further analysis. Calculation of the conversion-electron components overlaid in the electron spectra was performed using the PRINCEPS code[65], while the DDCM χ^2 fitting minimisation was performed employing the NAPATAU code[66].

Open ^{133}Ba and ^{207}Bi sources, and sealed ^{133}Ba and ^{152}Eu calibrated radioactive sources were used for electron and γ-ray energy and absolute efficiency calibrations, respectively, as explained in detail in refs. 54,57.

Data availability

The data obtained in the present work and the corresponding metadata are available from https://doi.org/10.23729/f2f0646a-40b5-4d74-9dca-d286945a68e6 (S24) and from https://doi.org/10.23729/01123445-a114-40c1-91d6-b51a25c076ea (JR161).

Received: 28 November 2024; Accepted: 20 December 2024;
Published online: 03 January 2025

References

1. Morinaga, H. Interpretation of some of the excited states of 4*n* self-conjugate nuclei. *Phys. Rev.* **101**, 254–258 (1956).
2. Garrett, P. E., Zielińska, M. & Clément, E. An experimental view on shape coexistence in nuclei. *Prog. Part. Nucl. Phys.* **124**, 103931 (2022).
3. Heyde, K. & Wood, J. L. Nuclear shapes: from earliest ideas to multiple shape coexisting structures. *Phys. Scr.* **91**, 083008 (2016).
4. Heyde, K. & Wood, J. L. Shape coexistence in atomic nuclei. *Rev. Mod. Phys.* **83**, 1467–1521 (2011).
5. Möller, P., Sierk, A. J., Bengtsson, R., Sagawa, H. & Ichikawa, T. Global calculation of nuclear shape isomers. *Phys. Rev. Lett.* **103**, 212501 (2009).
6. Andreyev, A. N. et al. A triplet of differently shaped spin-zero states in the atomic nucleus ^{186}Pb. *Nature* **405**, 430–433 (2000).
7. Ojala, J. et al. Reassigning the shapes of the 0^+ states in the ^{186}Pb nucleus. *Commun. Phys.* **5**, 213 (2022).

8. Julin, R., Grahn, T., Pakarinen, J. & Rahkila, P. In-beam spectroscopic studies of shape coexistence and collectivity in the neutron-deficient Z ≈ 82 nuclei. *J. Phys. G Nucl. Part. Phys.* **43**, 024004 (2016).
9. Julin, R., Helariutta, K. & Muikku, M. Intruder states in very neutron-deficient Hg, Pb and Po nuclei. *J. Phys. G Nucl. Part. Phys.* **27**, R109 (2001).
10. Egido, J. L., Robledo, L. M. & Rodríguez-Guzmán, R. R. Unveiling the origin of shape coexistence in lead isotopes. *Phys. Rev. Lett.* **93**, 082502 (2004).
11. Bender, M., Bonche, P., Duguet, T. & Heenen, P.-H. Configuration mixing of angular momentum projected self-consistent mean-field states for neutron-deficient Pb isotopes. *Phys. Rev. C* **69**, 064303 (2004).
12. Bonatsos, D., Karakatsanis, K. E., Martinou, A., Mertzimekis, T. J. & Minkov, N. Islands of shape coexistence from single-particle spectra in covariant density functional theory. *Phys. Rev. C* **106**, 044323 (2022).
13. Heyde, K. et al. A shell-model description of 0^+ intruder states in even-even nuclei. *Nucl. Phys. A* **466**, 189–226 (1987).
14. Heese, J. et al. Evidence for low-lying prolate bands in ^{188}Pb and ^{186}Pb. *Phys. Lett. B* **302**, 390–395 (1993).
15. Dracoulis, G. D. et al. Spectroscopy of $^{188}_{82}\mathrm{Pb}_{106}$: evidence for shape coexistence. *Phys. Rev. C* **69**, 054318 (2004).
16. Papadakis, P. et al. Direct observation of E0 transitions in ^{188}Pb through in-beam spectroscopy. *Phys. Lett. B* **858**, 139048 (2024).
17. Dracoulis, G. D. et al. Spherical and deformed isomers in ^{188}Pb. *Phys. Rev. C* **60**, 014303 (1999).
18. Dracoulis, G. D. et al. Isomer bands, E0 transitions, and mixing due to shape coexistence in $^{188}_{82}\mathrm{Pb}_{106}$. *Phys. Rev. C* **67**, 051301 (2003).
19. Bonn, J., Huber, G., Kluge, H.-J., Kugler, L. & Otten, E. Sudden change in the nuclear charge distribution of very light mercury isotopes. *Phys. Lett. B* **38**, 308–311 (1972).
20. Cocolios, T. E. et al. Early onset of ground state deformation in neutron deficient polonium isotopes. *Phys. Rev. Lett.* **106**, 052503 (2011).
21. Le Blanc, F. et al. Large odd-even radius staggering in the very light platinum isotopes from laser spectroscopy. *Phys. Rev. C* **60**, 054310 (1999).
22. Dinger, U. et al. Nuclear moments and change in the charge-radii of neutron deficient lead isotopes. *Z. Phys. A* **328**, 253–254 (1987).
23. Dutta, S. B. et al. Measurement of isotope shift and hyperfine splitting of $^{190, 191, 193, 197}$Pb isotopes by collinear laser spectroscopy. *Z. Phys. A* **341**, 39–45 (1991).
24. De Witte, H. et al. Nuclear charge radii of neutron-deficient lead isotopes beyond N = 104 midshell investigated by in-source laser spectroscopy. *Phys. Rev. Lett.* **98**, 112502 (2007).
25. Van Duppen, P. et al. Observation of low-lying $J^\pi = 0^+$ states in the single-closed-shell nuclei $_{192-198}$Pb. *Phys. Rev. Lett.* **52**, 1974–1977 (1984).
26. Pakarinen, J. et al. Collectivity in $^{196, 198}$Pb isotopes probed in coulomb-excitation experiments at REX-ISOLDE. *J. Phys. G: Nucl. Part. Phys.* **44**, 064009 (2017).
27. Pakarinen, J. et al. Evidence for prolate structure in light Pb isotopes from in-beam γ-ray spectroscopy of ^{185}Pb. *Phys. Rev. C* **80**, 031303 (2009).
28. Eskola, P. Compilation of data on alpha activities with Z > 50, N < 126. *Ark. Fys.* **36**, 477 (1967).
29. Roulet, C. et al. Properties of $^{192, 190}$Pb: behaviour of the very neutron-deficient even lead isotopes. *Nucl. Phys. A* **323**, 495–520 (1979).
30. May, F. R., Pashkevich, V. V. & Frauendorf, S. A prediction on the shape transitions in very neutron-deficient even-mass isotopes in the lead region. *Phys. Lett. B* **68**, 113–116 (1977).
31. Van Duppen, P., Coenen, E., Deneffe, K., Huyse, M. & Wood, J. L. Low-lying $J^\pi = 0^+$ states in ^{190,192}Pb populated in the α-decay of ^{194,196}Po. *Phys. Lett. B* **154**, 354–357 (1985).
32. Dendooven, P. et al. Life time measurements of 0^+ intruder states in ^{190,192,194}Pb. *Phys. Lett. B* **226**, 27–30 (1989).
33. Dracoulis, G. D., Byrne, A. P. & Baxter, A. M. Interference between spherical and deformed states in ^{190}Pb. *Phys. Lett. B* **432**, 37–44 (1998).
34. Wilson, A. N. et al. Observation of a superdeformed band in ^{190}Pb. *Eur. Phys. J. A* **24**, 179–183 (2005).
35. Cox, D. M. et al. Simulation of the SAGE spectrometer. *Eur. Phys. J. A* **51**, 64 (2015).
36. Sorri, J. et al. Determination of absolute internal conversion coefficients using the SAGE spectrometer. *Nucl. Instrum. Meth. A* **812**, 24–32 (2016).
37. Bateman, H. Solution of a system of differential equations occuring in the theory of radioactive transformations. *Proc. Cambridge Phil. Soc.* **15**, 423 (1910).
38. Dewald, A., Möller, O. & Petkov, P. Developing the recoil distance Doppler-shift technique towards a versatile tool for lifetime measurements of excited nuclear states. *Prog. Part. Nucl. Phys.* **67**, 786–839 (2012).
39. Grahn, T. et al. Collectivity and configuration mixing in ^{186,188}Pb and ^{194}Po. *Phys. Rev. Lett.* **97**, 062501 (2006).
40. Grahn, T. et al. Lifetimes of intruder states in ^{186}Pb, ^{188}Pb and ^{194}Po. *Nucl. Phys. A* **801**, 83–100 (2008).
41. Petkov, P., Dewald, A. & von Brentano, P. Gating on the feeding or on the depopulating transition in coincidence recoil-distance Doppler-shift lifetime measurements. *Nucl. Instrum. Methods Phys. Res. Sec. A* **457**, 527–530 (2001).
42. Hellemans, V., De Baerdemacker, S. & Heyde, K. Configuration mixing in the neutron-deficient $^{186-196}$Pb isotopes. *Phys. Rev. C* **77**, 064324 (2008).
43. Yao, J. M., Bender, M. & Heenen, P.-H. Systematics of low-lying states of even-even nuclei in the neutron-deficient lead region from a beyond-mean-field calculation. *Phys. Rev. C* **87**, 034322 (2013).
44. Nazarewicz, W. Variety of shapes in the mercury and lead isotopes. *Phys. Lett. B* **305**, 195–201 (1993).
45. Fossion, R., Heyde, K., Thiamova, G. & Van Isacker, P. Intruder bands and configuration mixing in lead isotopes. *Phys. Rev. C* **67**, 024306 (2003).
46. Smirnova, N. A., Heenen, P.-H. & Neyens, G. Self-consistent approach to deformation of intruder states in neutron-deficient Pb and Po. *Phys. Lett. B* **569**, 151–158 (2003).
47. Rodríguez-Guzmán, R. R., Egido, J. L. & Robledo, L. M. Beyond mean field description of shape coexistence in neutron-deficient Pb isotopes. *Phys. Rev. C* **69**, 054319 (2004).
48. Nomura, K., Rodríguez-Guzmán, R., Robledo, L. M. & Shimizu, N. Shape coexistence in lead isotopes in the interacting boson model with a Gogny energy density functional. *Phys. Rev. C* **86**, 034322 (2012).
49. Chasman, R. R., Egido, J. L. & Robledo, L. M. Persistence of deformed shapes in the neutron-deficient Pb region. *Phys. Lett. B* **513**, 325–329 (2001).
50. Dracoulis, G. D. et al. Effect of oblate deformation on E3 strengths in light lead and polonium isotopes. *Phys. Rev. C* **63**, 061302 (2001).
51. Carlsson, B. G., Toivanen, J. & Pastore, A. Collective vibrational states within the fast iterative quasiparticle random-phase approximation method. *Phys. Rev. C* **86**, 014307 (2012).
52. Church, E. L., Rose, M. E. & Weneser, J. Electric-monopole directional-correlation experiments. *Phys. Rev.* **109**, 1299–1306 (1958).
53. Dowie, J. T. H., Kibédi, T., Eriksen, T. K. & Stuchbery, A. E. Table of electronic factors for E0 electron and electron–positron pair conversion transitions. *At. Data Nucl. Data Tables* **131**, 101283 (2020).
54. Pakarinen, J. et al. The SAGE spectrometer. *Eur. Phys. J. A* **50**, 53 (2014).

55. Sarén, J. et al. The new vacuum-mode recoil separator MARA at JYFL. *Nucl. Instrum. Methods Res. Sec. B* **266**, 4196–4200 (2008).
56. Uusitalo, J., Sarén, J., Partanen, J. & Hilton, J. Mass analyzing recoil apparatus, MARA. *Acta Phys. Pol. B* **50**, 319 (2019).
57. Pakarinen, J. et al. The JUROGAM 3 spectrometer. *Eur. Phys. J. A* **56**, 149 (2020).
58. Uusitalo, J. et al. In-beam spectroscopy using the JYFL gas-filled magnetic recoil separator RITU. *Nucl. Instrum. Methods Res. Sec. B* **204**, 638–643 (2003).
59. Sarén, J., Uusitalo, J., Leino, M. & Sorri, J. Absolute transmission and separation properties of the gas-filled recoil separator RITU. *Nucl. Instrum. Methods Res. Sec. A* **654**, 508–521 (2011).
60. Plaza, A. M. et al. JYFL-ACCLAB-S24 In-beam spectroscopy of 190-Pb using the SAGE spectrometer at the MARA separator. University of Jyväskylä. https://doi.org/10.23729/f2f0646a-40b5-4d74-9dca-d286945a68e6 (2023).
61. Plaza, A. M. et al. JYFL-ACCLAB-JR161 Lifetime measurements of low-lying states in 190-Pb. University of Jyväskylä. https://doi.org/10.23729/01123445-a114-40c1-91d6-b51a25c076ea (2024).
62. Lazarus, I. et al. The GREAT triggerless total data readout method. *IEEE Trans. Nucl. Sci.* **48**, 567–569 (2001).
63. Rahkila, P. Grain—A Java data analysis system for total data readout. *Nucl. Instrum. Methods Res. Sec. A* **595**, 637–642 (2008).
64. Brun, R. & Rademakers, F. Root—An object oriented data analysis framework. *Nucl. Instrum. Methods Res. Sec. A* **389**, 81–86 (1997).
65. Plaza, A. M., Herzberg, R. D., Pakarinen, J. & Papadakis, P. PRINCEPS: towards the automation of simultaneous γ-ray and internal conversion electron analysis. *Acta Phys. Pol. B Proc. Suppl.* **17**, 3–A11 (2024).
66. Saha, B. Bestimmung der lebensdauern kollektiver kernanregungen in 124-Xe und entwicklung von entsprechender analysesoftware. *Ph.D. thesis, Universität zu Köln.* http://kups.ub.uni-koeln.de/id/eprint/1246 (2004).

Acknowledgements

This project has received funding from the European Union's Horizon Europe Research and Innovation programme under Grant Agreement No. 101057511. The authors also thank the GAMMAPOOL European Spectroscopy Resource for the loan of the detectors for the JUROGAM 3 array. Support from the Science and Technology Facilities Council (UK) Grants No. ST/P004598/1 and ST/V001027/1, and the German Research Foundation (Deutsche Forschungsgemeinschaft, DFG), Grant No. FR 3276/3-1 is acknowledged. We thank Karl-Oskar Zell for making the ^{108}Pd target. A.I. acknowledges funding from the European Union's Horizon 2020 research and innovation programme under the Marie Skodowska-Curie Grant Agreement No. 847635. O.A.S. acknowledges funding from the Spanish MCIN/AEI/10.13039/501100011033 under Grant PID2021-126998OB-I00. B.S.N.S. acknowledges the financial support of the UKRI STFC through Grants No. ST/T001739/1 and ST/P005101/1. A.R. acknowledges the Academy of Finland Project No. 339245. M.S. acknowledges the Academy of Finland Project No. 354968 and the European Union's Horizon 2020 research and innovation programme under Grant Agreement No. 771036 (ERC CoG MAIDEN). A.R. and J.W. acknowledge the European Union's Horizon 2020 research and innovation programme under Grant Agreement No. 861198-LISA-H2020-MSCA-ITN-2019.

Author contributions

J.P. and R.-D.H. prepared the proposal for the S24 experiment. A.M.P., J.P. and J.O. prepared the proposal for the JR161 experiment. A.M.P., J.P., A.D.B., A.I. and J.O. set up the instrumentation for the S24 experiment. A.M.P., J.P., A.I., P.Ruotsalainen and E.U. set up the instrumentation for the JR161 experiment. A.M.P., J.P., P.P., R.-D.H., R.J., A.D.B., A.I., J.O., P.Ruotsalainen, K.A., T.G., P.T.G., H.Joukainen, H.Jutila, M.Leino, J.L., M.Luoma, P.Rahkila, J.R., J.S., M.S, A.T.-D., J.U. and G.L.Z. monitored the detector, data acquisition and beam systems during the S24 experiment. A.M.P., J.P., P.P., R.-D.H., R.J., A.D.B., A.I., J.O., P.Ruotsalainen, E.U., B.A., A.A., O.A.-S., K.A., V.B., J.C., A.E., C.F., T.G., P.T.G., J.J., H.Joukainen, H.Jutila, C.-D.L., M.Leino, J.L., M.Luoma, A.M., B.S.N.S., P.Rahkila, A.R., J.R., J.S., M.-M.S., M.S, C.M.S., J.U., F.V.S., J.W. and G.L.Z. monitored the detector, data acquisition and beam systems during the JR161 experiment. A.M.P., J.P., P.P., R.-D.H., R.J. and T.R.R. carried out the data analysis and interpretation of the data. A.M.P., J.P., P.P., R.-D.H., R.J. and T.R.R. prepared the manuscript.

Competing interests

The authors declare no competing interests.

Additional information

Supplementary information The online version contains supplementary material available at https://doi.org/10.1038/s42005-024-01928-8.

Correspondence and requests for materials should be addressed to Janne Pakarinen.